

Mapping Enzymatic Catalysis using the Effective Fragment Molecular Orbital Method: Towards all ab initio Biochemistry

Casper Steinmann¹, Dmitri G. Fedorov², Jan H. Jensen^{1,*}

1 Department of Chemistry, University of Copenhagen, Universitetsparken 5, DK-2100 Copenhagen, Denmark

2 NRI, National Institute of Advanced Industrial Science and Technology (AIST), 1-1-1 Umezono, Tsukuba, Ibaraki 305-8568, Japan

* corresponding author, E-mail: jhjensen@chem.ku.dk

Abstract

We extend the Effective Fragment Molecular Orbital (EFMO) method to the frozen domain approach where only the geometry of an active part is optimized, while the many-body polarization effects are considered for the whole system. The new approach efficiently mapped out the entire reaction path of chorismate mutase in less than four days using 80 cores on 20 nodes, where the whole system containing 2398 atoms is treated in the ab initio fashion without using any force fields. The reaction path is constructed automatically with the only assumption of defining the reaction coordinate a priori. We determine the reaction barrier of chorismate mutase to be 18.3 ± 3.5 kcal mol⁻¹ for MP2/cc-pVDZ and 19.3 ± 3.6 for MP2/cc-pVTZ in an ONIOM approach using EFMO-RHF/6-31G(d) for the high and low layers, respectively.

Introduction

Fragment-based quantum mechanical methods [1–12] are becoming increasingly popular [13], and have been used to describe a very diverse set of molecular properties for large systems. Although these methods have been applied to refine the energetics of some enzymatic reactions [14,15] they are usually not efficient enough to allow for many hundreds of single point calculations needed to map out a reaction path for a system containing thousands of atoms, although geometry optimizations of large systems can be performed for systems consisting of several hundreds of atoms [8,9,11,16–18]. In fact, typically applications of fragment-based methods to biochemical systems, for example, to protein-ligand binding [19], are based on performing a few single point calculations for structures obtained at a lower level of theory (such as with force fields). Although many force fields are well tuned to treat typical proteins, for ligands they can be problematic.

In this work we extend the effective fragment molecular orbital (EFMO) method [20,21] into the frozen domain (FD) formalism [18], originally developed for the fragment molecular orbital (FMO) method [22–25]. For FMO, there is also partial energy gradient method [26].

EFMO is based on dividing a large molecular system into fragments and performing ab initio calculations of fragments and their pairs, and combining their energies in the energy of the whole system (see more below). In the FD approach we employ here, one defines an active region associated with the active site, and the cost of a geometry optimization is then essentially given by the cost associated with the active region.

However, unlike the quantum-mechanical / molecular mechanical (QM/MM) method [27] with non-polarizable force fields, the polarization of the whole system is accounted for in FMO and EFMO methods: in the former via the explicit polarizing potential and in the latter via fragment polarizabilities. Another important difference between EFMO and QM/MM is that the former does not involve force fields, and the need to elaborately determine parameters for ligands does not exist in EFMO. Also, in EFMO all fragments are treated with quantum mechanics, and the problem of the active site size [28] does not arise.

The paper is organized as follows: First, we derive the EFMO energy and gradient expressions for the frozen domain approach, when some part of the system is frozen during the geometry optimization. Secondly, we predict the reaction barrier of the conversion of chorismate to prephenate (Figure 1) in chorismate mutase. The reaction has been studied previously using conventional QM/MM techniques [29–40]. The EFMO method is similar in spirit to QM/MM in using a cheap model for the less important part of the system and the mapping is accomplished with a reasonable amount of computational resources (four days per reaction path using 80 CPU cores). Finally we summarize our results and discuss future directions.

Background and Theory

The EFMO energy of a system of N fragments (monomers) is

$$E^{\text{EFMO}} = \sum_I^N E_I^0 + \sum_{IJ}^{R_{I,J} \leq R_{\text{resdim}}} (\Delta E_{IJ}^0 - E_{IJ}^{\text{POL}}) + \sum_{IJ}^{R_{I,J} > R_{\text{resdim}}} E_{IJ}^{\text{ES}} + E_{\text{tot}}^{\text{POL}} \quad (1)$$

where E_I^0 is the gas phase energy of monomer I . The second sum in equation 1 is the pairwise correction to the monomer energy and only applies for pairs of fragments (dimers) separated by an interfragment distance $R_{I,J}$ (defined previously [20]) less than a threshold R_{resdim} . The correction for dimer IJ is

$$\Delta E_{IJ}^0 = E_{IJ}^0 - E_I^0 - E_J^0. \quad (2)$$

E_{IJ}^{POL} and $E_{\text{tot}}^{\text{POL}}$ are the classical pair polarization energy of dimer IJ and the classical total polarization energy, respectively. Both energies are evaluated using the induced dipole model [41, 42] based on distributed polarizabilities [43]. The final sum over E_{IJ}^{ES} is the classical electrostatic interaction energy and applies only to dimers separated by a distance greater than R_{resdim} . These energies are evaluated using atom-centered multipole moments through quadrupoles [44]. The multipole moments and distributed polarizabilities are computed on the fly for each fragment [20, 21].

In cases where only part of a molecular system is to be optimized by minimizing the energy, equation 1 can be rewritten, resulting in a method conceptually overlapping with QM/MM in using a cheap model for the less important part of the system. Consider a system S (Figure 2) where we wish to optimize the positions of atoms in region A , while keeping the atoms in region b and F frozen (the difference between b and F will be discussed below). With this definition, we rewrite the EFMO energy as

$$E^{\text{EFMO}} = E_F^0 + E_b^0 + E_A^0 + E_{F/b}^0 + E_{F/A}^0 + E_{A/b}^0 + E_{\text{tot}}^{\text{POL}}, \quad (3)$$

where E_A^0 is the internal energy of region A . Region A is made of fragments containing atoms whose position is optimized, and A can also have some frozen atoms

$$E_A^0 = \sum_{I \in A}^N E_I^0 + \sum_{I, J \in A}^{R_{I, J} \leq R_{\text{resdim}}} (\Delta E_{IJ}^0 - E_{IJ}^{\text{POL}}) + \sum_{I, J \in A}^{R_{I, J} > R_{\text{resdim}}} E_{IJ}^{\text{ES}}. \quad (4)$$

Similarly, E_b^0 is the internal energy of b

$$E_b^0 = \sum_{I \in b}^N E_I^0 + \sum_{I, J \in b}^{R_{I, J} \leq R_{\text{resdim}}} (\Delta E_{IJ}^0 - E_{IJ}^{\text{POL}}) + \sum_{I, J \in b}^{R_{I, J} > R_{\text{resdim}}} E_{IJ}^{\text{ES}}, \quad (5)$$

Region A is surrounded by a buffer b , because fragment pairs computed with QM containing one fragment outside of A (i.e., in b) can still contribute to the total energy gradient (see below). On the other hand,

fragment pairs with one fragment in F can also contribute to the total gradient, but they are computed using a simple classical expression rather than with QM. Note that the relation between the notation used in FMO/FD and that we use here is as follows: A, F and S are the same. The buffer region B includes A , but b does not, i.e., A and b share no atoms. Formally, A and b are always treated at the same level of theory by assigning fragments to the same layer.

In the EFMO method, covalent bonds between fragments are not cut. Instead, electrons from a bond connecting two fragments are placed entirely to one of the fragments. The electrons of the fragments are kept in place by using frozen orbitals across the bond. [21, 45, 46] Fragments connected by a covalent bond share atoms (Figure 3) through the bonding region so it is possible that one side changes the wave function of the bonding region [21]. It is therefore necessary to re-evaluate the internal *ab initio* energy of region b for each new geometry step.

The internal geometries of fragments in region F are completely frozen so the internal energy is constant and is therefore neglected

$$E_F^0 = 0. \quad (6)$$

However, it is still necessary to compute the multipole moments and polarizability tensors (and therefore the wave function) of the fragments in F once at the beginning of a geometry-optimization to evaluate $E_{\text{tot}}^{\text{POL}}$ in equation 3 as well as some inter-region interaction energies defined as

$$E_{b/A}^0 = \sum_{\substack{I \in b \\ J \in A}}^{R_{I,J} \leq R_{\text{resdim}}} (\Delta E_{IJ}^0 - E_{IJ}^{\text{POL}}) + \sum_{\substack{I \in b \\ J \in A}}^{R_{I,J} > R_{\text{resdim}}} E_{IJ}^{\text{ES}}, \quad (7)$$

$$E_{F/A}^0 = \sum_{\substack{I \in A \\ J \in F}} E_{IJ}^{\text{ES}}, \quad (8)$$

$$E_{F/b}^0 = 0. \quad (9)$$

Equation 8 assumes that b is chosen so that fragments in A and F are sufficiently separated (i.e., $R_{I,J} > R_{\text{resdim}}$) so the interaction is evaluated classically. If all atoms in region b are frozen, then $E_{F/b}^0$ is constant and can be neglected. However, this assumes that the positioins of all atoms at both sides of the bonds connecting fragments are frozen.

The final expression for the EFMO frozen domain (EFMO/FD) energy is

$$E^{\text{EFMO}} = E_b^0 + E_A^0 + E_{b/A}^0 + \sum_{\substack{I \in A \\ J \in F}}^{R_{I,J} > R_{\text{resdim}}} E_{IJ}^{\text{ES}} + E_{\text{tot}}^{\text{POL}}. \quad (10)$$

Finally, we note that due to the frozen geometry of b we can further gain a speedup by not evaluating dimers in b (cross terms between A and b are handled explicitly according to equation 7) since they do not contribute to the energy or gradient of A . This corresponds to the frozen domain with dimers (EFMO/FDD), and equation 5 becomes

$$E_b^0 = \sum_{I \in b}^N E_I^0. \quad (11)$$

The gradient of each region is

$$\frac{\partial E^{\text{EFMO}}}{\partial x_A} = \frac{\partial E_A^0}{\partial x_A} + \frac{\partial E_{A/b}^0}{\partial x_A} + \frac{\partial E_{A/F}^0}{\partial x_A} + \frac{\partial E_{\text{tot}}^{\text{POL}}}{\partial x_A}, \quad (12)$$

$$\frac{\partial E^{\text{EFMO}}}{\partial x_b} = 0, \quad (13)$$

$$\frac{\partial E^{\text{EFMO}}}{\partial x_F} = 0, \quad (14)$$

and the details of their evaluation has been discussed previously [20,21]. Equation 13 does not apply to non-frozen atoms shared with region A .

The frozen domain formulation of EFMO was implemented in GAMESS [47] and parallelized using the generalized distributed data interface [48,49].

Computational Details

Preparation of the Enzyme Model

We followed the strategy by Claeysens *et al.* [40] The structure of chorismate mutase (PDB: 2CHT) solved by Chook *et al.* [50] was used as a starting point. Chains A, B and C were extracted using PyMOL [51] and subsequently protonated with PDB2PQR [52,53] and PROPKA [54] at pH = 7. The protonation state of all residues can be found in Table S1. The inhibitor between chain A and C was replaced with chorismate in the reactant state (**1**, Figure 1) modeled in Avogadro [55,56].

The entire complex (chorismate mutase and chorismate) was solvated in water (TIP3P [57]) using GROMACS. [58,59] To neutralize the system 11 Na^+ counter ions were added. The protein and counter ions were treated with the CHARMM27 [60,61] force field in GROMACS. Force-field parameters for chorismate were generated using the SwissParam [62] tool. To equilibrate the complex a 100 ps NVT run at $T = 300\text{ K}$ was followed by a 100 ps NPT run at $P = 1\text{ bar}$ and $T = 300\text{ K}$. The production run was an isothermal-isobaric trajectory run for 10 ns. A single conformation was randomly selected from the last half of the simulation and energy minimized in GROMACS to a force threshold of $F_{\text{max}} = 300\text{ KJ mol}^{-1}\text{ nm}^{-1}$. During equilibration and final molecular dynamics (MD) simulation, the C3 and C4 atoms of chorismate (see Figure 1) were harmonically constrained to a distance of 3.3 \AA to keep it in the reactant state. Finally, a sphere of 16 \AA around the C1 atom of chorismate was extracted in PyMOL and hydrogens were added to correct the valency where the backbone was cut. The final model contains a total of 2398 atoms.

Mapping the Reaction Path

To map out the reaction path, we define the reaction coordinate similarly to Claeysens *et al.* [40] as the difference in bond length between the breaking O2-C1 bond and the forming C4-C3 bond in chorismate (see also Figure 1), i.e.

$$R = R_{21} - R_{43}. \quad (15)$$

The conversion of chorismate ($R = -2.0\text{ \AA}$, $R_{21} = 1.4\text{ \AA}$, $R_{43} = -3.4\text{ \AA}$) to prephenate ($R = 1.9\text{ \AA}$, $R_{21} = 3.3\text{ \AA}$, $R_{43} = 1.4\text{ \AA}$) in the enzyme was mapped by constraining the two bond lengths in equation 15 with a harmonic force constant of $500\text{ kcal mol}^{-1}\text{ \AA}^{-2}$ in steps of 0.1 \AA . For each step, all atoms in the active region (A) were minimized to a threshold on the gradient of $5.0 \cdot 10^{-4}\text{ Hartree Bohr}^{-1}$ (OPTTOL=5.0e-4 in \$STATPT). For the enzyme calculations we used EFMO-RHF and FMO2-RHF with the frozen domain approximation presented above.

We used two different sizes for the active region small: (EFMO:S, Figure 4) and large (EFMO:L, Figure 5). The active region (colored red in Figure 2) is defined as all fragments with a minimum distance R_{active} from any atom in chorismate (EFMO:S : $R_{\text{active}} = 2.0\text{ \AA}$, EFMO:L : $R_{\text{active}} = 3.0\text{ \AA}$). In EFMO:S the active region consists of chorismate, 4 residues and 5 water molecules, while the active region in EFMO:L consists of chorismate, 11 residues and 4 water molecules. The buffer region (blue in

Figure 2) is defined as all fragments within 2.5 Å of the active region for both EFMO:S and EFMO:L. The rest of the system is frozen. To prepare the input files we used FragIt [63], which automatically divides the system into fragments; in this work we used the fragment size of one amino acid residue or water molecule per fragment.

In order to refine the energetics, for each minimized step on the reaction path we performed two-layer ONIOM [64,65] calculations

$$E_{\text{real}}^{\text{high}} \approx E_{\text{real}}^{\text{low}} + E_{\text{model}}^{\text{high}} - E_{\text{model}}^{\text{low}}, \quad (16)$$

where $E_{\text{real}}^{\text{low}} = E^{\text{EFMO}}$ according to equation 3. This can be considered a special case of the more general multicenter ONIOM based on FMO [66], using EFMO instead of FMO. The high level model system is chorismate in the gas-phase calculated using B3LYP [67–69] (DFTTYP=B3LYP in \$CONTRL) or MP2 (MPLEVL=2 in \$CONTRL) with either 6-31G(d) or the cc-pVDZ, cc-pVTZ and cc-pVQZ basis sets by Dunning [70].

We also carried out multilayer EFMO and FMO [71] single-point calculations where region F is described by RHF/6-31G(d) and b and A (for EFMO) or B ($B = A \cup b$ for FMO [18]) is calculated using MP2/6-31G(d).

The FDD approximation in equation 11 is enabled by specifying MODFD=3 in \$FMO, similarly to the frozen domain approach in FMO [18]. All calculations had spherical contaminants removed from the basis set (ISPHER=1 in \$CONTRL).

Obtaining the Activation Enthalpy

The activation enthalpy is obtained in two different ways by calculating averages of M adiabatic reaction pathways. The starting points of the M pathways were randomly extracted from the MD simulation, followed by the reaction path mapping procedure described above for each pathway individually. One way to obtain the activation enthalpy averages the barriers from each individual adiabatic reaction path [72]

$$\Delta H_1^\ddagger = \frac{1}{M} \sum_{i=1}^M (E_{\text{TS},i} - E_{\text{R},i}) - 1.6 \text{ kcal mol}^{-1}. \quad (17)$$

Here M is the number of reaction paths ($M = 7$, Figure 6) $E_{\text{TS},i}$ is the highest energy on the adiabatic reaction path while $E_{\text{R},i}$ is the lowest energy with a negative reaction coordinate. 1.6 kcal mol⁻¹ corrects

for the change in zero point energy and thermal contributions [72].

The other way of estimating the activation enthalpy is [37]:

$$\Delta H_2^\ddagger = \langle E_{\text{TS}} \rangle - \langle E_{\text{R}} \rangle - 1.6 \text{ kcal mol}^{-1}. \quad (18)$$

Here $\langle E_{\text{TS}} \rangle$ and $\langle E_{\text{R}} \rangle$ are, respectively, the highest energy and lowest energy with a negative reaction coordinate on the averaged adiabatic path (bold line in Figure 6). The brackets here mean averaging over 7 reaction paths; and the difference of Eqs 17 and 18 arises because of the noncommutativity of the sum and the min/max operation over coordinates: in Eq 17 we found a minimum and a maximum for each curve separately, and averaged the results, but in Eq 18 we first averaged and then found the extrema. As discussed below, the two reaction enthalpies are within 0.2 kcal/mol, which indicates that the TS occurs at roughly the same value of the reaction coordinate for most paths.

Results and Discussion

Effects of Methodology, Region Sizes and Approximations

Reaction barriers obtained in the enzyme using harmonic constraints are plotted on Figure 8 and listed in Table 1 for different settings of region sizes and approximations. All calculated reaction barriers are within 0.5 kcal mol⁻¹ from each other when going from the reactant (R_{R}) to the proposed transition (R_{TS}) state where the reaction barriers for the TSs are around 46 kcal mol⁻¹. The same is true when going to the product R_{P} . Only the large model (EFMO:L) shows a difference in energy near the product (R_{P}) with a lowering of the relative energy by 4 kcal mol⁻¹ compared to the other settings.

The reaction coordinates are also similar for the small systems ($R_{\text{P}} = 1.41 \text{ \AA}$, except for $R_{\text{resdim}} = 2.0$ which is $R_{\text{P}} = 1.56 \text{ \AA}$) with some minor kinks on the energy surface from optimization of the structures without constraints at R_{P} . The EFMO:L model has a different reaction coordinate for the product ($R_{\text{P}} = 1.57 \text{ \AA}$) and also a shifted reaction coordinate for the transition state $R_{\text{TS}} = -0.12 \text{ \AA}$ which we can attribute to a better description of more separated pairs in the active region but more importantly that around the TS, the energy surface is very flat. Interestingly, using FMO2 shows no significant change in either reaction barriers or reaction coordinates for the reactant, transition state or product which differ from EFMO:S by 0.02 \AA , 0.03 \AA and 0.01 \AA respectively. Timings are discussed below.

Previous work by Ranaghan *et al.* [36,37] obtained an RHF barrier of 36.6 kcal mol⁻¹ which is 10 kcal/mol lower than what we obtained. Also, they observed that the transition state happened earlier at $R_{TS} = -0.3$ Å. The difference in reaction barrier from our findings is attributed to a poorer enzyme structure and other snapshots do yield similar or better reaction barriers (see below). Furthermore, the same study by Ranaghan *et al.* found that the reaction is indeed exothermic with a reaction energy of around -30 kcal mol⁻¹ at the RHF/6-31G(d) level of theory. We expect this difference from our results to arise from the fact the study by Ranaghan *et al.* used a fully flexible model for both the substrate and the enzyme where the entire protein is free to adjust contrary to our model where we have chosen active fragments and atoms in a uniform sphere around a central fragment. This is perhaps not the best solution if one includes too few fragments (which lowers the computational cost) due to fragments in the buffer region are unable to move and cause steric clashes. The lowering of the energy for EFMO:L suggests this.

Refined Reaction Energetics

For the smallest EFMO:S system ONIOM results are presented on Figure 9 and in Table 2 for various levels of theory. By calculating the MP2/cc-pVDZ:EFMO-RHF/6-31G(d) energy using ONIOM we obtain a 19.8 kcal mol⁻¹ potential energy barrier. Furthermore, the reaction energy is lowered from -1.3 kcal mol⁻¹ to -5.5 kcal mol⁻¹. Increasing the basis set size through cc-pVTZ and cc-pVQZ reduces the barrier to 21.8 kcal mol⁻¹ and 21.7 kcal mol⁻¹, respectively and the reaction energy is -1.1 kcal mol⁻¹ and 0.8 kcal mol⁻¹. Using the smaller 6-31G(d) basis set with MP2, the reaction barrier is 22.2 kcal mol⁻¹ and reaction energy is -3.2 kcal mol⁻¹. The B3LYP results are improvements for the TS only reducing the barrier to 23.8 kcal mol⁻¹ for B3LYP/cc-pVDZ:EFMO-RHF/6-31G(d). The same is not true for the product where the energy is increased by about 3 kcal mol⁻¹. For the other systems treated using EFMO-RHF/6-31G(d) discussed in the previous section ONIOM corrected results at the MP2 or B3LYP level of theory using a cc-pVDZ basis set are listed in tables S2 to S5 and show differences from the above by less than 1 kcal mol⁻¹, again the reaction coordinates changes slightly depending on the system. The effect of including correlation effects by means of MP2 and systematically larger basis sets is that the potential energy barrier for the reaction rises as more correlation effects are included, the same is true for the overall reaction energy.

The results presented here for MP2 are in line with what has been observed previously by Ranaghan

et al. [37] and Claeysens *et al.* [40]. Overall, the reaction barrier is reduced to roughly half of the RHF barrier and the observed coordinates for the reaction shift slightly. We do note that this study and the study by Ranaghan *et al.* use ONIOM style energy corrections for the correlation and not geometry optimizations done at a correlated level. Overall, we observe that the predicted reaction coordinate for the approximate transition state in the conversion of chorismate to prephenate happens around 0.2 Å later than in those studies.

The results for the multilayer single points along the energy surface are presented in Table 3. The barrier calculated at the EFMO-RHF:MP2/6-31G(d) level of theory is predicted to be 27.6 kcal mol⁻¹ which is 5.4 kcal mol⁻¹ higher than the ONIOM barrier and the reaction coordinates are shifted for both the reactant and the TS from $R_R = -1.95$ Å to $R_R = -1.64$ Å and $R_{TS} = -0.36$ Å to $R_{TS} = -0.11$ Å. Similar results are obtained at the FMO2-RHF:MP2/6-31G(d) level of theory. The difference from the ONIOM corrected values in table 3 is likely due to the inclusion of dispersion effects between the chorismate and the enzyme which is apparently weaker at the transition state compared to the reactant state.

Ensemble Averaging

In Figure 6 and Figure 7 we show 7 adiabatic reaction paths mapped with EFMO-RHF/6-31G(d) starting from 7 MD snapshots; the energetics were refined with ONIOM at the MP2/cc-pVDZ and MP2/cc-pVTZ level. In EFMO, we used a small active region (EFMO:S) and $R_{\text{resdim}} = 1.5$ and no dimer calculations in region *b* (S15FD3 in Figure 8). Out of the 7 trajectories one is described in detail in the previous sub-section.

For MP2/cc-pVDZ:EFMO-RHF/6-31G(d) the reaction enthalpies are $\Delta H_1^\ddagger = 18.3 \pm 3.5$ kcal mol⁻¹ and $\Delta H_2^\ddagger = 18.2$ kcal mol⁻¹ [cf. Equations (17) and (18)], the latter having an uncertainty of the mean of 6.9 kcal mol⁻¹. For MP2/cc-pVTZ:EFMO-RHF/6-31G(d) the reaction enthalpies are $\Delta H_1^\ddagger = 19.3 \pm 3.7$ kcal mol⁻¹ and $\Delta H_2^\ddagger = 18.8$ kcal mol⁻¹ with an uncertainty of the mean of 7.1 kcal mol⁻¹. These barriers are ca 5.5 (6.5) kcal mol⁻¹ higher than the experimental value of 12.7 ± 0.4 kcal mol⁻¹ for MP2/cc-pVDZ (MP2/cc-pVTZ). For comparison, the activation enthalpy obtained by Claeysens *et al.* [40,72] (9.7 ± 1.8 kcal mol⁻¹) is underestimated by 3.0 kcal mol⁻¹.

There are several differences between our study and that of Claeysens *et al.* that could lead to an overestimation of the barrier height: biasing the MD towards the TS rather than the reactant, a larger

enzyme model (7218 vs 2398 atoms), and more conformational freedom when computing the potential energy profile.

With regard to the latter point, while Figure 8 shows that increasing the active region has a relatively small effect on the barrier this may not be the case for all snapshots. We did identify one trajectory that failed to produce a meaningful reaction path and is presented in Figure S1. Here, the energy of the barrier becomes unrealistically high because of very little flexibility in the active site and unfortunate placement of Phe57 (located in the buffer region, Figure S2), which hinders the conformational change needed for the successful conversion to prephenate yielding an overall reaction energy of around +11 kcal mol⁻¹. As noted above, the EFMO:L settings is a possible solution to this as more of the protein is available to move, but as seen from Table 1 the computational cost doubles.

Timings

Using the computationally most efficient method tested here (EFMO:S), $R_{\text{resdim}} = 1.5$, and skipping dimers in the buffer region b , an adiabatic reaction path, which requires a total of 467 gradient evaluations, can be computed in four days using 80 CPU cores (20 nodes with 4 cores each) at the RHF/6-31G(d) level of theory. As shown in Table 1, the same calculation using FMO2 requires takes roughly $T_{\text{rel}}^{\text{full}} = 7.5$ times longer.

Increasing R_{resdim} from 1.5 to 2 has a relatively minor effect of the CPU time (a factor of 1.2), while performing the dimer calculations in the buffer region nearly doubles (1.7) the CPU time. Similarly, increasing the size of active region from 2.0 Å to 3.0 Å around chorismate also nearly doubles (1.8) the CPU time. This is mostly due to the fact that more dimer calculations must be computed, but the optimizations also require more steps (513 gradient evaluations) to converge due to the larger number of degrees of freedom that must be optimized.

Looking at a single minimization for a specific reaction coordinate $R = -1.79$ Å, the most efficient method takes 4.5 hours. Here, the relative timings T_{rel} are all larger than for the full run ($T_{\text{rel}}^{\text{full}}$) due to a slight increase in the number of geometry steps (around 25) taken for all but FMO2 which is identical to the reference (22 steps). Thus, the overall cost of performing the FMO2 minimization is 6.7 times as expensive as EFMO.

Summary and Outlook

In this paper we have shown that the effective fragment molecular orbital (EFMO) method [20,21] can be used to efficiently map out enzymatic reaction paths provided the geometry of a large part of the enzyme and solvent is frozen. In EFMO one defines an active region associated with the active site, and the cost of a geometry optimization is then essentially the cost of running quantum-mechanical calculations of the active domain. This is similar to the cost of QM/MM, if the QM region is the same; the difference is that in EFMO we freeze the coordinates of the rest of the system, whereas in QM/MM they are usually fully relaxed. On the other hand, EFMO does not require parameters and can be better considered an approximation to a full QM calculation rather than a QM/MM approach.

In this work we used the mapping technique based on running a classical MD simulation, selecting some trajectories, freezing the coordinates of the outside region, and doing constrained geometry optimizations along a chosen reaction coordinate. An alternative to this approach is to run full MD simulation of a chemical reaction using EFMO. This has already been done for many chemical reactions using FMO-MD [73–75] and can be done in future with EFMO.

A potential energy profile for the chorismate to prephenate reaction in chorismate has been computed in 4 days using 80 CPU cores for an RHF/6-31G(d) description of a truncated model of the enzyme containing 2398 atoms. For comparison, a corresponding FMO2 calculation takes about 7.5 times more. The cost of EFMO calculations is mainly determined by the size of the buffer- and active region. Comparing to a QM/MM with QM region of the same size, EFMO as a nearly linear scaling method, becomes faster than QM if the system size is sufficiently large; especially for correlated methods like MP2 where this cross-over should happen with relatively small sizes.

Our computed conformationally-averaged activation enthalpy is in reasonable agreement to the experimental value, although overestimated by 5.5 kcal/mol.

The energetics of this reaction depends on the level of calculation. We have shown that by using a level better than RHF, for instance, MP2 or DFT, considerably improves the energetics and by using such an appropriate level to also determine the reaction path following the formalism in this work can be used to provide a general and reliable way in future.

EFMO, as one of the fragment-based methods [13], can be expected to be useful in various biochemical studies, such as in enzymatic catalysis and protein-ligand binding. It should be noted that in addition to

its parameter-free ab initio based nature, EFMO and FMO also offer chemical insight on the processes by providing subsystem information, such as the properties of individual fragments (e.g., the polarization energy) as well as the pair interaction energies between fragments [76, 77]. This can be of considerable use to fragment-based drug discovery [78, 79].

Acknowledgements

CS and JHJ thank the Danish Center for Scientific Computing at the University of Copenhagen for providing computational resources. DGF thanks the Next Generation Super Computing Project, Nanoscience Program (MEXT, Japan) and Strategic Programs for Innovative Research (SPIRE, Japan).

References

1. Otto P, Ladik J (1975) Investigation of the interaction between molecules at medium distances: I. SCF LCAO MO supermolecule, perturbational and mutually consistent calculations for two interacting HF and CH₂O molecules. *Chem Phys* 8: 192-200.
2. Gao J (1997) Toward a molecular orbital derived empirical potential for liquid simulations. *J Phys Chem B* 101: 657-663.
3. Hua S, Xu L, Li W, Li S (2011) Cooperativity in long α - and 3_{10} -helical polyalanines: Both electrostatic and van der waals interactions are essential. *J Phys Chem B* 115: 11462-11469.
4. Leverentz HR, Maerzke KA, Keasler SJ, Siepmann JI, Truhlar DG (2012) Electrostatically embedded many-body method for dipole moments, partial atomic charges, and charge transfer. *Phys Chem Chem Phys* 14: 7669-7678.
5. Frankcombe TJ, Collins MA (2012) Growing fragmented potentials for gas-surface reactions: The reaction between hydrogen atoms and hydrogen-terminated silicon (111). *J Phys Chem C* 116: 7793-7802.
6. Huang L, Massa L (2012) Quantum kernel applications in medicinal chemistry. *Fut Med Chem* 4: 1479-1494.

7. Söderhjelm P, Kongsted J, Ryde U (2010) Ligand affinities estimated by quantum chemical calculations. *J Chem Theory Comput* 6: 1726-1737.
8. Furtado JP, Rahalkar AP, Shanker S, Bandyopadhyay P, Gadre SR (2012) Facilitating minima search for large water clusters at the mp2 level via molecular tailoring. *J Phys Chem Lett* 3: 2253-2258.
9. Liu K, Inerbaev T, Korchowiec J, Gu FL, Aoki Y (2012) Geometry optimization for large systems by the elongation method. *Theor Chem Acc* 131: 1277.
10. Saparpakorn P, Kobayashi M, Hannongbua S, Nakai H (2013) Divide-and-conquer-based quantum chemical study for interaction between hiv-1 reverse transcriptase and mk-4965 inhibitor. *Int J Quantum Chem* : in press.
11. Guo W, Wu A, Zhang IY, Xu X (2012) XO: An extended ONIOM method for accurate and efficient modeling of large systems. *J Comput Chem* 33: 2142-2160.
12. Antony J, Grimme S (2012) Fully ab initio protein-ligand interaction energies with dispersion corrected density functional theory. *J Comput Chem* 33: 1730-1739.
13. Gordon MS, Fedorov DG, Pruitt SR, Slipchenko LV (2012) Fragmentation methods: A route to accurate calculations on large systems. *Chem Rev* 112: 632-672.
14. Ishida T, Fedorov DG, Kitaura K (2006) All electron quantum chemical calculation of the entire enzyme system confirms a collective catalytic device in the chorismate mutase reaction. *J Phys Chem B* 110: 1457-1463.
15. Polyakov IV, Grigorenko BL, Moskovsky AA, Pentkovski VM, Nemukhin AV (2012) Towards quantum-based modeling of enzymatic reaction pathways: Application to the acetylcholinesterase catalysis. *Chem Phys Lett* : in press.
16. Fedorov DG, Ishida T, Uebayasi M, Kitaura K (2007) The fragment molecular orbital method for geometry optimizations of polypeptides and proteins. *J Phys Chem A* 111: 2722-32.
17. Nagata T, Fedorov DG, Li H, Kitaura K (2012) Analytic gradient for second order møller-plesset perturbation theory with the polarizable continuum model based on the fragment molecular orbital method. *J Chem Phys* 136: 204112.

18. Fedorov DG, Alexeev Y, Kitaura K (2011) Geometry optimization of the active site of a large system with the fragment molecular orbital method. *J Phys Chem Lett* 2: 282–288.
19. Sawada T, Fedorov DG, Kitaura K (2010) Role of the key mutation in the selective binding of avian and human influenza hemagglutinin to sialosides revealed by quantum-mechanical calculations. *J Am Chem Soc* 132: 16862-16872.
20. Steinmann C, Fedorov DG, Jensen JH (2010) Effective fragment molecular orbital method: A merger of the effective fragment potential and fragment molecular orbital methods. *J Phys Chem A* 114: 8705–8712.
21. Steinmann C, Fedorov DG, Jensen JH (2012) The effective fragment molecular orbital method for fragments connected by covalent bonds. *PLoS ONE* 7: e41117.
22. Kitaura K, Ikeo E, Asada T, Nakano T, Uebayasi M (1999) Fragment molecular orbital method: an approximate computational method for large molecules. *Chem Phys Lett* 313: 701-706.
23. Fedorov DG, Kitaura K (2007) Extending the power of quantum chemistry to large systems with the fragment molecular orbital method. *J Phys Chem A* 111: 6904-6914.
24. Fedorov DG, Kitaura K, editors (2009) *The Fragment Molecular Orbital Method: Practical Applications to Large Molecular Systems*. Boca Raton, FL: CRC Press.
25. Fedorov DG, Nagata T, Kitaura K (2012) Exploring chemistry with the fragment molecular orbital method. *Phys Chem Chem Phys* 14: 7562-7577.
26. Ishikawa T, Yamamoto N, Kuwata K (2010) Partial energy gradient based on the fragment molecular orbital method: Application to geometry optimization. *Chem Phys Lett* 500: 149-154.
27. Gao J, Truhlar DG (2002) Quantum mechanical methods for enzyme kinetics. *Annu Rev Phys Chem* 53: 467-505.
28. Hu LH, Eliasson J, Heimdal J, Ryde U (2009) Do quantum mechanical energies calculated for small models of protein-active sites converge? *J Phys Chem A* 113: 11793-11800.
29. Lyne PD, Mulholland AJ, Richards WG (1995) Insights into chorismate mutase catalysis from a combined qm/mm simulation of the enzyme reaction. *J Am Chem Soc* 117: 11345–11350.

30. Davidson MM, Gould IR, Hillier IH (1996) The mechanism of the catalysis of the claisen rearrangement of chorismate to prephenate by the chorismate mutase from bacillus subtilis. a molecular mechanics and hybrid quantum mechanical/molecular mechanical study. *J Chem Soc, Perkin Trans 2* : 525–532.
31. Hall RJ, Hindle SA, Burton NA, Hillier IH (2000) Aspects of hybrid QM/MM calculations: the treatment of the QM/MM interface region and geometry optimization with an application to chorismate mutase. *J Comput Chem* 21: 1433–1441.
32. Marti S, Andres J, Moliner V, Silla E, Tuñón I, et al. (2001) Transition structure selectivity in enzyme catalysis: a QM/MM study of chorismate mutase. *Theor Chem Acc* 105: 207–212.
33. Worthington SE, Roitberg AE, Krauss M (2001) An MD/QM Study of the Chorismate Mutase-Catalyzed Claisen Rearrangement Reaction. *J Phys Chem B* 105: 7087–7095.
34. Lee YS, Worthington SE, Krauss M, Brooks BR (2002) Reaction mechanism of chorismate mutase studied by the combined potentials of quantum mechanics and molecular mechanics. *J Phys Chem B* 106: 12059–12065.
35. Lee Woodcock H, Hodošček M, Sherwood P, Lee YS, Schaefer Iii HF, et al. (2003) Exploring the quantum mechanical/molecular mechanical replica path method: a pathway optimization of the chorismate to prephenate claisen rearrangement catalyzed by chorismate mutase. *Theor Chem Acc* 109: 140–148.
36. Ranaghan KE, Ridder L, Szefczyk B, Sokalski WA, Hermann JC, et al. (2003) Insights into enzyme catalysis from QM/MM modelling: transition state stabilization in chorismate mutase. *Mol Phys* 101: 2695–2714.
37. Ranaghan KE, Ridder L, Szefczyk B, Sokalski WA, Hermann JC, et al. (2004) Transition state stabilization and substrate strain in enzyme catalysis: ab initio qm/mm modelling of the chorismate mutase reaction. *Org Biomol Chem* 2: 968–980.
38. Friesner RA, Guallar V (2005) Ab initio quantum chemical and mixed quantum mechanics/molecular mechanics (QM/MM) methods for studying enzymatic catalysis. *Annu Rev Phys Chem* 56: 389–427.

39. Crespo A, Martí MA, Estrin DA, Roitberg AE (2005) Multiple-steering QM-MM calculation of the free energy profile in chorismate mutase. *J Am Chem Soc* 127: 6940–6941.
40. Claeysens F, Ranaghan KE, Lawan N, Macrae SJ, Manby FR, et al. (2011) Analysis of chorismate mutase catalysis by qm/mm modelling of enzyme-catalysed and uncatalysed reactions. *Org Biomol Chem* 9: 1578–1590.
41. Day PN, Jensen JH, Gordon MS, Webb SP, Stevens WJ, et al. (1996) An effective fragment method for modeling solvent effects in quantum mechanical calculations. *J Chem Phys* 105: 1968–1986.
42. Gordon MS, Freitag MA, Bandyopadhyay P, Jensen JH, Kairys V, et al. (2001) The effective fragment potential method: A QM-based MM approach to modeling environmental effects in chemistry. *J Phys Chem A* 105: 293–307.
43. Minikis RM, Kairys V, Jensen JH (2001) Accurate intraprotein electrostatics derived from first principles: an effective fragment potential method study of the proton affinities of lysine 55; tyrosine 20 in turkey ovomucoid third domain. *J Phys Chem A* 105: 3829–3837.
44. Stone AJ (1981) Distributed multipole analysis, or how to describe a molecular charge distribution. *Chem Phys Lett* 83: 233–239.
45. Fedorov DG, Jensen JH, Deka RC, Kitaura K (2008) Covalent bond fragmentation suitable to describe solids in the fragment molecular orbital method. *J Phys Chem A* 112: 11808–11816.
46. Fedorov D, Avramov P, Jensen J, Kitaura K (2009) Analytic gradient for the adaptive frozen orbital bond detachment in the fragment molecular orbital method. *Chem Phys Lett* 477: 169–175.
47. W. SM, Baldrige KK, Boatz JA, Elbert S, Gordon MS, et al. (1993) General atomic molecular electronic structure system. *J Comput Chem* 14: 1347–1363.
48. Fedorov DG, Kitaura K (2004) The importance of three-body terms in the fragment molecular orbital method. *J Chem Phys* 120: 6832–6840.
49. Fedorov DG, Olson RM, Kitaura K, Gordon MS, Koseki S (2004) A new hierarchical parallelization scheme: Generalized distributed data interface (GDDI), and an application to the fragment molecular orbital method (FMO). *J Comput Chem* 25: 872–880.

50. Chook YM, Ke H, Lipscomb WN (1993) Crystal structures of the monofunctional chorismate mutase from bacillus subtilis and its complex with a transition state analog. *Proc Nat Acad Sci USA* 90: 8600.
51. Schrodinger L (2010) The pymol molecular graphics system. Version 1: r1.
52. Dolinsky TJ, Nielsen JE, McCammon JA, Baker NA (2004) PDB2PQR: an automated pipeline for the setup of Poisson–Boltzmann electrostatics calculations. *Nucleic Acids Res* 32: W665.
53. Dolinsky TJ, Czodrowski P, Li H, Nielsen JE, Jensen JH, et al. (2007) PDB2PQR: expanding and upgrading automated preparation of biomolecular structures for molecular simulations. *Nucleic Acids Res* 35: W522.
54. Li H, Robertson AD, Jensen JH (2005) Very fast empirical prediction and rationalization of protein pka values. *Proteins* 61: 704–721.
55. Avogadro v.1.0.3. Accessed 2012 Aug 1.
56. Hanwell MD, Curtis DE, Lonie DC, Vandermeersch T, Zurek E, et al. (2012) Avogadro: An advanced semantic chemical editor, visualization, and analysis platform. *J Cheminform* 4: 17.
57. Jorgensen WL, Chandrasekhar J, Madura JD, Impey RW, Klein ML (1983) Comparison of simple potential functions for simulating liquid water. *J Chem Phys* 79: 926–935.
58. Van Der Spoel D, Lindahl E, Hess B, Groenhof G, Mark AE, et al. (2005) GROMACS: fast, flexible, and free. *J Comput Chem* 26: 1701–1718.
59. Hess B, Kutzner C, Van Der Spoel D, Lindahl E (2008) Gromacs 4: Algorithms for highly efficient, load-balanced, and scalable molecular simulation. *J Chem Theory Comput* 4: 435–447.
60. MacKerell AD, Banavali N, Foloppe N (2000) Development and current status of the CHARMM force field for nucleic acids. *Biopolymers* 56: 257–265.
61. Brooks BR, Brooks CL, Mackerell AD, Nilsson L, Petrella RJ, et al. (2009) CHARMM: The biomolecular simulation program. *J Comput Chem* 30: 1545–1614.
62. Zoete V, Cuendet MA, Grosdidier A, Michielin O (2011) Swissparam: A fast force field generation tool for small organic molecules. *J Comput Chem* .

63. Steinmann C, Ibsen M, Hansen AS, Jensen JH (2012) Fragit: A tool to prepare input files for fragment based quantum chemical calculations. PLoS ONE 7: e44480.
64. Svensson M, Humbel S, Froese RDJ, Matsubara T, Sieber S, et al. (1996) ONIOM: A multilayered integrated MO+ MM method for geometry optimizations and single point energy predictions. A test for Diels-Alder reactions and $\text{Pt}(\text{P}(t\text{-Bu})_3)_2 + \text{H}_2$ oxidative addition. J Phys Chem 100: 19357–19363.
65. Dapprich S, Komáromi I, Byun KS, Morokuma K, Frisch MJ (1999) A new ONIOM implementation in Gaussian98. Part I. The calculation of energies, gradients, vibrational frequencies and electric field derivatives. J Mol Struct 461: 1–21.
66. Asada N, Fedorov DG, Kitaura K, Nakanishi I, K. M. Merz J (2012) An efficient method to evaluate intermolecular interaction energies in large systems using overlapping multicenter oniom and the fragment molecular orbital method. J Phys Chem Lett 3: 2604-2610.
67. Becke AD (1993) A new mixing of hartree–fock and local density-functional theories. J Phys Chem 98: 5648-5652.
68. Stephens PJ, Devlin FJ, Chabalowski CF, Frisch MJ (1994) Ab initio calculation of vibrational absorption and circular dichroism spectra using density functional force fields. J Phys Chem 98: 11623-11627.
69. Hertwig RH, Koch W (1997) On the parameterization of the local correlation functional. What is Becke-3-LYP? Chem Phys Lett 268: 345–351.
70. Dunning Jr TH (1989) Gaussian basis sets for use in correlated molecular calculations. I. The atoms boron through neon and hydrogen. J Chem Phys 90: 1007.
71. Fedorov DG, Ishida T, Kitaura K (2005) Multilayer formulation of the fragment molecular orbital method (FMO). J Phys Chem A 109: 2638–2646.
72. Claeysens F, Harvey JN, Manby FR, Mata RA, Mulholland AJ, et al. (2006) High-accuracy computation of reaction barriers in enzymes. Angew Chem 118: 7010–7013.

73. Komeiji Y, Nakano T, Fukuzawa K, Ueno Y, Inadomi Y, et al. (2003) Fragment molecular orbital method: application to molecular dynamics simulation, 'ab initio FMO-MD'. *Chem Phys Lett* 372: 342-347.
74. Sato M, Yamataka H, Komeiji Y, Mochizuki Y, Ishikawa T, et al. (2008) How does an S_N2 reaction take place in solution? Full ab initio MD simulations for the hydrolysis of the methyl diazonium ion. *J Am Chem Soc* 130: 2396-2397.
75. Komeiji Y, Mochizuki Y, Nakano T, Mori H (2012) Recent advances in fragment molecular orbital-based molecular dynamics (FMO-MD) simulations. In: Wang L, editor, *Molecular Dynamics - Theoretical Developments and Applications in Nanotechnology and Energy*, Intech. pp. 3-24.
76. Fedorov DG, Kitaura K (2007) Pair interaction energy decomposition analysis. *J Comput Chem* 28: 222-237.
77. Fedorov DG, Kitaura K (2012) Energy decomposition analysis in solution based on the fragment molecular orbital method. *J Phys Chem A* 116: 704-719.
78. Murray CW, Blundell TL (2010) Structural biology in fragment-based drug design. *Curr Opin Struct Biol* 20: 497-507.
79. Alexeev Y, Mazanetz MP, Ichihara O, Fedorov DG (2012) GAMESS as a free quantum-mechanical platform for drug research. *Curr Top Med Chem* : in press.

1 Figures

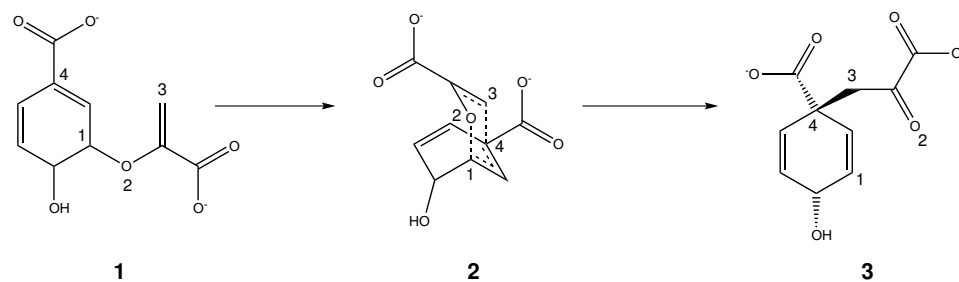


Figure 1. Conversion of chorismate to prephenate through its transition state. Atoms of interest are marked with numbers one through four.

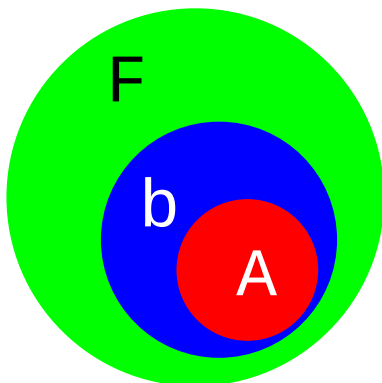


Figure 2. Definition of a system with active, buffer and frozen regions in frozen domain EFMO.

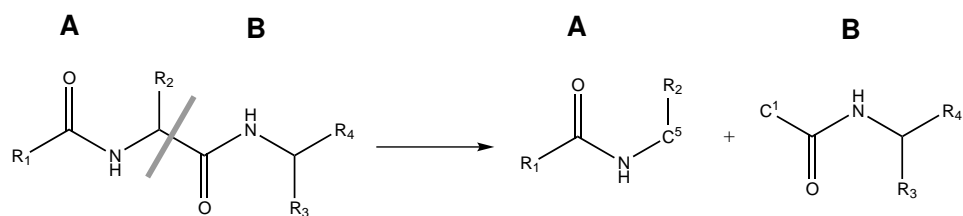


Figure 3. Cross region fragmentation. The fragmentation procedure shares an atom (here C¹ and C⁵ is the shared atom) between two neighboring and covalently bonded fragments. Even though these fragments are in separate regions, they still share an atom across that region as illustrated.

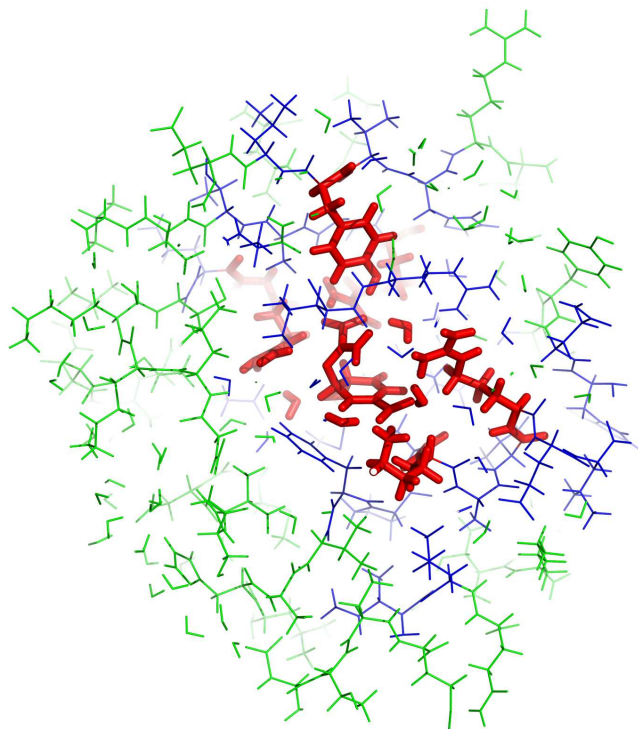


Figure 4. EFMO:S model of chorismate mutase used in this study. The entire model contains 2398 atoms. There are 1341 atoms in green belonging to the frozen region (F), 928 atoms in blue belonging to the buffer region (b) and 129 atoms in red belonging to the active region (A).

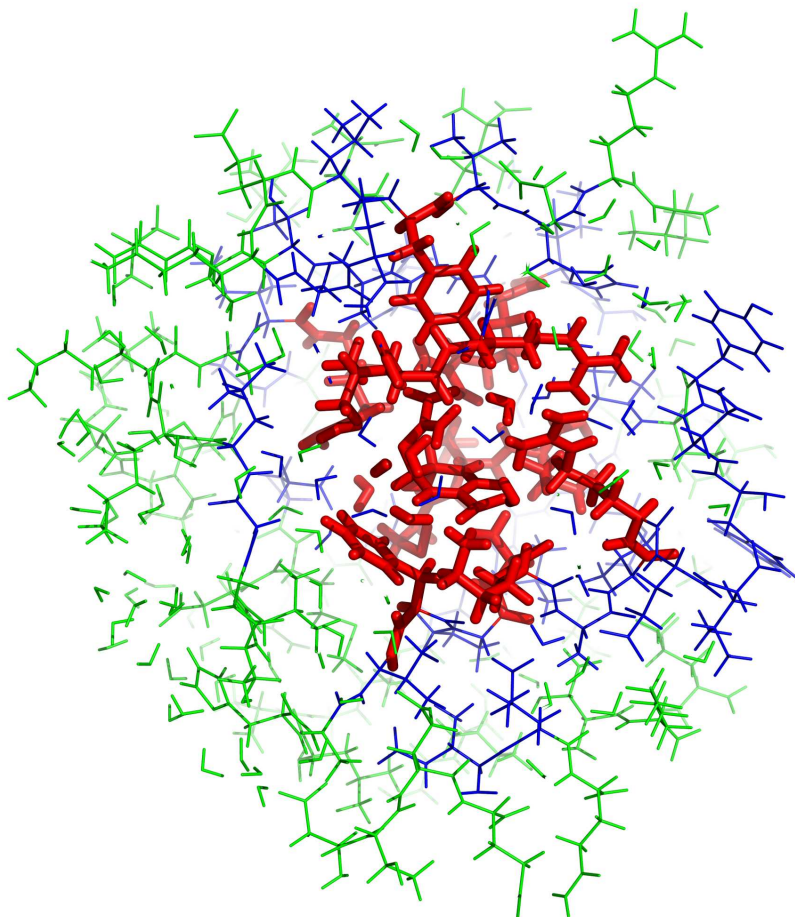


Figure 5. EFMO:L model of chorismate mutase used in this study. The entire model contains 2398 atoms. There are 1006 atoms in green belonging to the frozen region (F), 1151 atoms in blue belonging to the buffer region (b) and 241 atoms in red belonging to the active region (A).

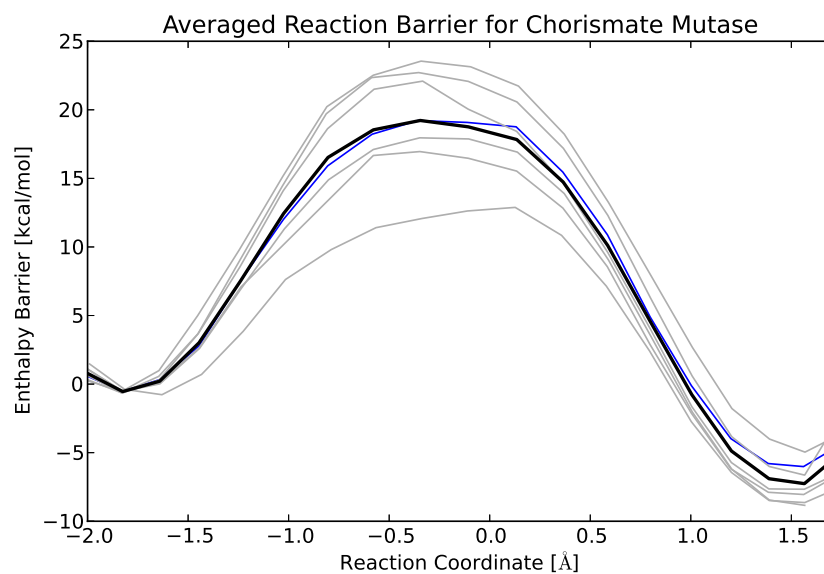


Figure 6. Reaction Enthalpy Profile for chorismate mutase. The 7 profiles are calculated with ONIOM at the MP2/cc-pVDZ:EFMO-RHF/6-31G(d) level of theory. The black line is the average reaction energy, grey lines are individual reaction paths. The blue line is the reaction path discussed in detail, in the results section.

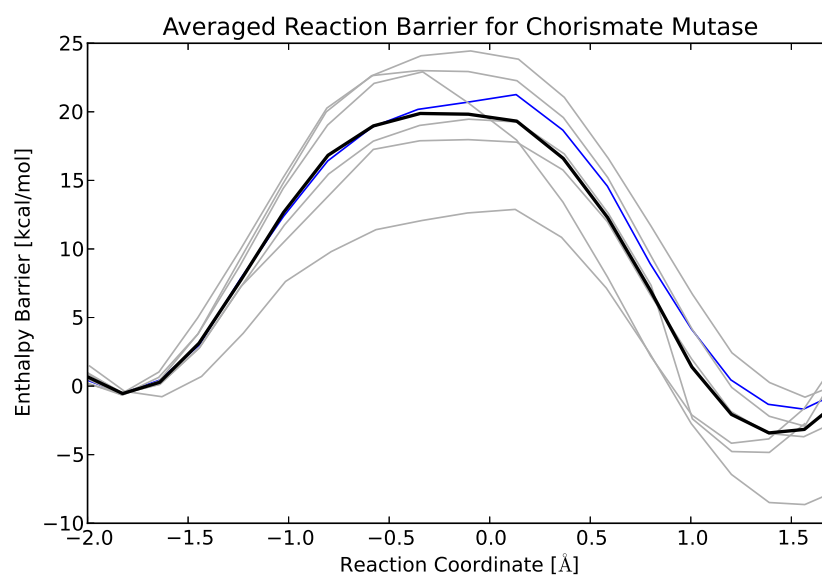


Figure 7. Reaction Enthalpy Profile for chorismate mutase. The 7 profiles are calculated with ONIOM at the MP2/cc-pVTZ:EFMO-RHF/6-31G(d) level of theory. The black line is the average reaction energy, grey lines are individual reaction paths. The blue line is the reaction path discussed in detail, in the results section.

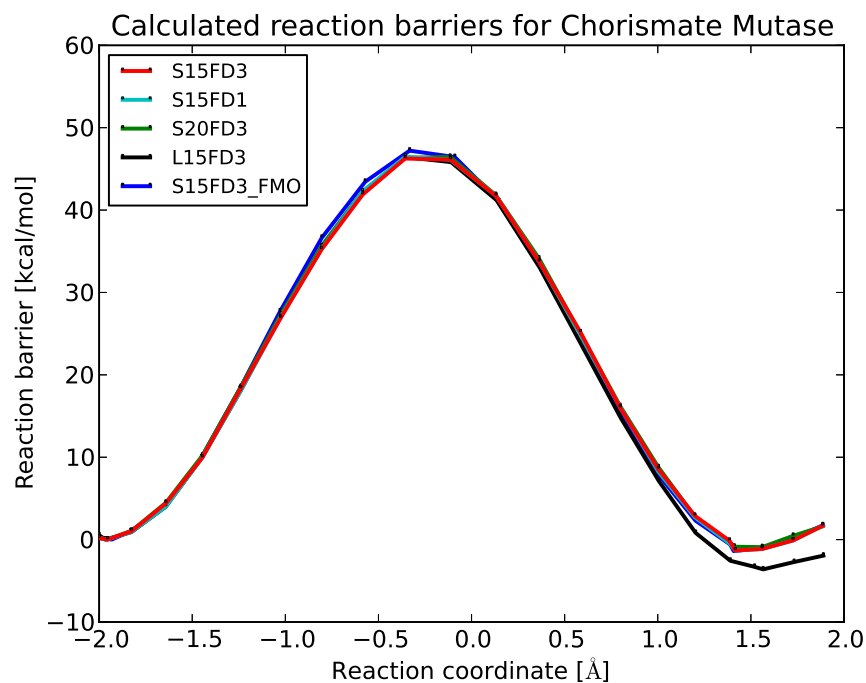


Figure 8. EFMO-RHF/6-31G(d) barrier for chorismate mutase. S15FD3 and S15FD3_FMO are EFMO:S and FMO:S, respectively, both with $R_{\text{resdim}} = 1.5$, and the dimer approximation in region b (Equation 11). S15FD1 is similar to S15FD3 but without the dimer approximation in region b . S20FD3 is also similar to S15FD3 but with $R_{\text{resdim}} = 2.0$, instead. Finally, L15FD3 is EFMO:L with $R_{\text{resdim}} = 1.5$, and the dimer approximation (FDD) in region b .

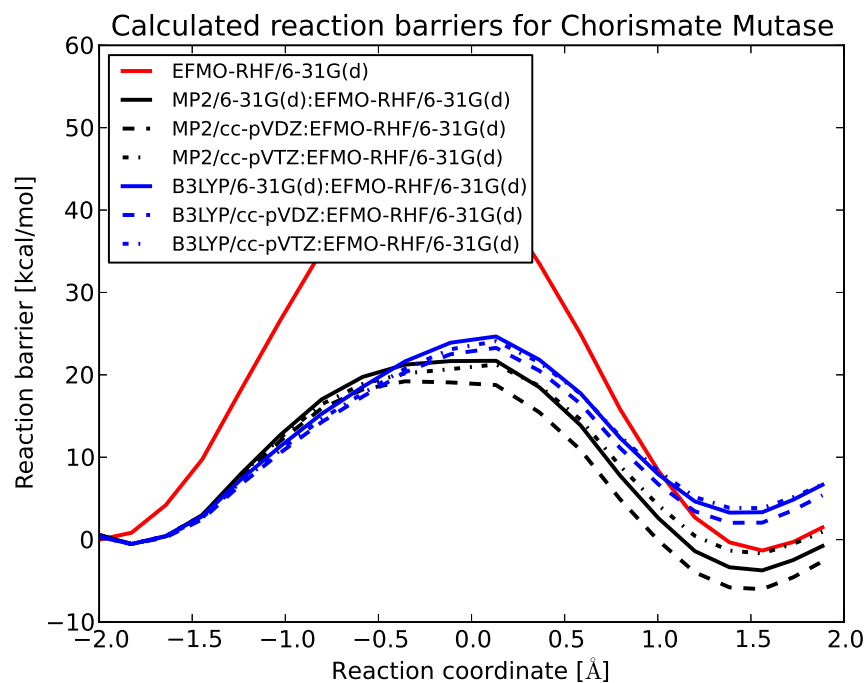


Figure 9. ONIOM results calculated with various levels of theory for EFMO:S geometries. The red curve is the EFMO-RHF/6-31G(d) result also presented in Figure 8. Blue (B3LYP) and green (MP2) curves are ONIOM results with chorismate calculated in the gas-phase using the 6-31G(d) (solid lines), cc-pVDZ (dashed lines) or cc-pVTZ (dotted line) basis set.

2 Tables

Table 1. EFMO-RHF and FMO2-RHF results for chorismate mutase.

Model	R_{resdim}	modfd	R_R	R_{TS}	R_P	E_{TS-R}	E_{P-R}	T_{rel}	T_{rel}^{full}
EFMO: S	1.5	3	-1.95	-0.36	1.42	46.25	-1.32	1.0	1.0
EFMO: S	1.5	1	-1.96	-0.36	1.42	46.49	-1.34	2.0	1.7
EFMO: S	2.0	3	-1.96	-0.12	1.56	46.46	-0.91	1.3	1.2
EFMO: L	1.5	3	-1.97	-0.35	1.57	46.42	-3.61	2.1	1.8
FMO2: S	1.5	3	-1.93	-0.33	1.41	47.21	-1.40	6.7	7.5

Reaction barriers of chorismate mutase calculated with different levels of theory. R_{resdim} is unitless. The reaction coordinates for the reactant, transition state and product are R_R , R_{TS} and R_P , respectively and given in Å, barrier height of the transition state E_{TS-R} and overall reaction energy E_{P-R} in kcal/mol. T_{rel} are relative timings to EFMO-RHF/6-31G(d) using the EFMO:**S** model with the fully minimized reaction coordinate on the trajectory subject to harmonic constraints. T_{rel}^{full} are for the entire path.

Table 2. Reaction barriers of chorismate mutase calculated using ONIOM.

	R_R	R_{TS}	R_P	E_{TS-R}	E_{P-R}
MP2/6-31G(d)	-1.83	0.13	1.56	22.24	-3.20
MP2/cc-pVDZ	-1.83	-0.36	1.56	19.75	-5.48
MP2/cc-pVTZ	-1.83	0.13	1.56	21.79	-1.14
MP2/cc-pVQZ	-1.83	0.13	1.56	21.68	-0.82
B3LYP/6-31G(d)	-1.83	0.13	1.39	25.19	3.81
B3LYP/cc-pVDZ	-1.83	0.13	1.39	23.81	2.58
B3LYP/cc-pVTZ	-1.83	0.13	1.56	24.62	4.36
B3LYP/cc-pVQZ	-1.83	0.13	1.56	24.66	4.16

The reaction coordinates in Å for the reactant, transition state and product are R_R , R_{TS} and R_P , respectively. The barrier height of the transition state E_{TS-R} and the overall reaction energy E_{P-R} are in kcal/mol.

Table 3. Reaction barriers of chorismate mutase calculated using multilayer EFMO and FMO2 calculations.

	R_R	R_{TS}	R_P	E_{TS-R}	E_{P-R}
EFMO-RHF:MP2/6-31G(d)	-1.64	-0.11	1.39	27.64	-4.70
FMO2-RHF:MP2/6-31G(d)	-1.64	-0.11	1.88	29.22	-6.41

The reaction coordinates in Å for the reactant, transition state and product are R_R , R_{TS} and R_P , respectively. The barrier height of the transition state E_{TS-R} and the overall reaction energy E_{P-R} are in kcal/mol.

Supporting Information

Figure S1. Reaction barrier calculated at the MP2/cc-pVDZ:EFMO-RHF/6-31G(d) level of theory for EFMO:S using $R_{\text{resdim}} = 1.5$ and FDD (modfd=3). This snapshot shows the effect of not having enough flexibility in the active region around the substrate.

Figure S2. Two different starting geometries with chorismate and Phe57 shown as sticks from the MD simulation. A) shows a configuration which results in a successful reaction path and B) a configuration which results in an unsuccessful reaction path (see Figure S1). The position of Phe57 coupled with a placement in the buffer region (*b*) makes it unable to move to accomodate the conversion of chorismate to prephenate.

Table S1. Complete listing of all residues in the protein model (PDB: 2CHT) along with their protonation state after being protonated using the PDB2PQR tool.

Table S2. Reaction barriers of chorismate mutase calculated using ONIOM for EFMO:S using $R_{\text{resdim}} = 1.5$ and FD (modfd=1).

Table S3. Reaction barriers of chorismate mutase calculated using ONIOM for EFMO:S using $R_{\text{resdim}} = 2.0$ and FDD (modfd=3).

Table S4. Reaction barriers of chorismate mutase calculated using ONIOM for EFMO:L using $R_{\text{resdim}} = 1.5$ and FDD (modfd=3).

Table S5. Reaction barriers of chorismate mutase calculated using ONIOM for FMO2:S using $R_{\text{resdim}} = 1.5$ and FDD (modfd=3).